Characterisation and Investigation of Inorganic Scintillation Detectors with Radioactive Sources

Matthew Brown

Nuclear Physics
Laboratory Project

School of Physics and Astronomy
University of Birmingham
October 2023

Abstract

The resolution and efficiencies of five different diameter and length, cylindrical NaI(Tl) scintillators (0.55″ x 1.69″, 1″ x 1″, 2″ x 2″, 3″ x 3″ and 4.49″ x 4.49″) have been compared for γ-ray energies from 59.5 keV to 1337 keV along with their photopeak-to-Compton ratios at 662 keV. Negligible relationship was found between NaI(Tl) detector size and resolution, especially at lower energy values. The largest and smallest detectors showed the worst resolution, which has been attributed to non-proportionality of light yield. The resolution of the largest detector seems to be worsened significantly more by this non-proportionality than Poisson statistical broadening due to its shallower gradient of -0.246 ± 0.008 on a log scale plot. Efficiency and photopeak-to-Compton ratio clearly increased with increasing crystal size due to the capture of more Compton scattering events in larger detectors. Again, the largest detector was an outlier and had lower values for these two parameters than the 3″ x 3″ detector, further suggesting some defective behaviour inside. The nature of anode and dynode voltage signals were explored using a self-activated $CeBr_3$ detector. The last-dynode-to-anode gain was found to be 4.82 ± 0.03 at the nominal -1000 V supply and the decay time of the anode pulse was calculated to be approximately half that of the dynode, at 13.47 ± 0.08 μs.

Keywords: NaI(Tl), energy resolution, intrinsic efficiency, photopeak-to-Compton ratio, anode.

1 Introduction

Despite its discovery in 1948, thallium doped sodium iodide, NaI(Tl), crystals remain one of the most common choices of scintillation materials today. Scintillators are widely used in γ-ray, x-ray and charged particle detection in areas from experimental particle physics, to medical diagnosis in computed tomography [1]. This makes understanding their properties particularly important for the development of new scintillation materials that would be advantageous in specific cases, and for the comparison of different types and sizes to assess their suitability for a particular use. In our laboratory are many different sizes of NaI(Tl) detectors and of different ages, meaning their characterisation is furthermore needed to assess their performance and usability for current experiments. The aim of this investigation therefore was to characterise five different sized cylindrical NaI(Tl) scintillation detectors by examining their resolutions and efficiencies as a function of γ-ray energy and to compare their photopeak-to-Compton ratios at 662 keV. Additionally, the difference between anode and dynode signals was to be explored to highlight certain scenarios where the anode signal could be preferred over last-dynode signals.

2 Detector Overview

2.1 Scintillator Properties

At the front of each detector is the inorganic NaI scintillator crystal, cylindrical in shape of varying diameter and length, where ionizing radiation first enters leading to the production of visible light. Scintillation crystals may be organic or inorganic, and their type depends on what is to be detected; inorganic crystals are typically of high density and are favoured for the detection of gamma rays, whereas organic scintillators are used in fast neutron detection and particle physics experiments due to their faster decay time [2][3]. Decay time in the context of scintillators refers to the time elapsed to the point at which the intensity of the light pulse generated in the medium has fallen to 1/e of its maximum value, typically hundreds of ns, and

is dependent on temperature as demonstrated by J.S. Schweitzer and W. Ziehl in NaI(Tl) [4].

The energy states of the scintillation crystal dictates the production of visible light; the lower valence band is where electrons are bound to lattice sites, and the conduction band is where electrons have sufficient energy to traverse through the scintillator. An incoming γ-ray, typically several hundreds to thousands of keVs, enters the crystal and may be absorbed by an electron in the valence band. The band gap for NaI is ~5.89 eV, hence upon absorption of a γ-ray, an electron in the valence band will be removed entirely with high kinetic energy, leaving a hole in the valence band [5]. The free electron loses energy by exciting ions in its path as it travels through the crystal. Upon de-excitation, the electron returns to the valence band, recombining with a hole, and emits a photon with an energy equal to the band gap. For the NaI crystal, this is ultra-violet light, which the scintillator itself is not transparent to. As a result, this photon will be absorbed by another electron in the valence band to be promoted to the conduction band. This process would continuously repeat, which is also a very inefficient process. To combat this, one introduces energy levels in the forbidden band gap by doping the scintillator crystal, in this case with thallium hence the notation *NaI(Tl)*. These added impurities are called activators, and since they introduce energy levels in-between the valence and conduction bands, the de-excitation of free electrons through these levels can result in the emission of visible light photons. The de-excitation through the activator energy levels can occur across a time scale on the order of 30-500 ns [2].

2.2 Gamma-ray Interactions in Scintillators

Only three mechanisms for γ-ray interactions with matter are most important in this investigation; photoelectric absorption, Compton scattering and pair production. Pair production occurs above twice the rest-mass energy of an electron, at 1.022 MeV, and the probability of this occurring at a few hundred keV above this value is low [2]. Instead, γ-rays with energies of several MeV will more likely interact in this way. This is beyond the energy range of this investigation, (where full-energy peaks will at most be ~1.3 MeV), and hence Compton scattering and photoelectric absorption remain as the two most dominant processes. As discussed above, γ-rays may deposit all their energy in photoelectric absorption leading to the entire removal of an electron from the valence band. The probability of this interaction is proportional to $E^{-3.5}$, and is therefore more dominant at lower energies. At higher energies, the probability of Compton scattering dominates, since the probability of this interaction is proportional to E^{-1}. This process results in an electron recoiling from an incident photon which subsequently scatters at an angle with a lower energy. This process can repeat for high energy photons, up to a point where it will be photoelectrically absorbed. Figure 2.1 illustrates the cross sections of the competing processes as a function of photon energy.

Compton scattering introduces the Compton continuum which represents the range of energies that an electron can possess after the process. The end of the continuum represents the maximum energy of an electron where an incident γ-ray to the scintillator scatters 180°, and hence higher energy photopeaks will sit beyond the continuum. A backscatter peak is also visible on top of the continuum at lower energies, and occurs due to γ-rays backscattering from inside the detector, and into the scintillator, depositing energy.

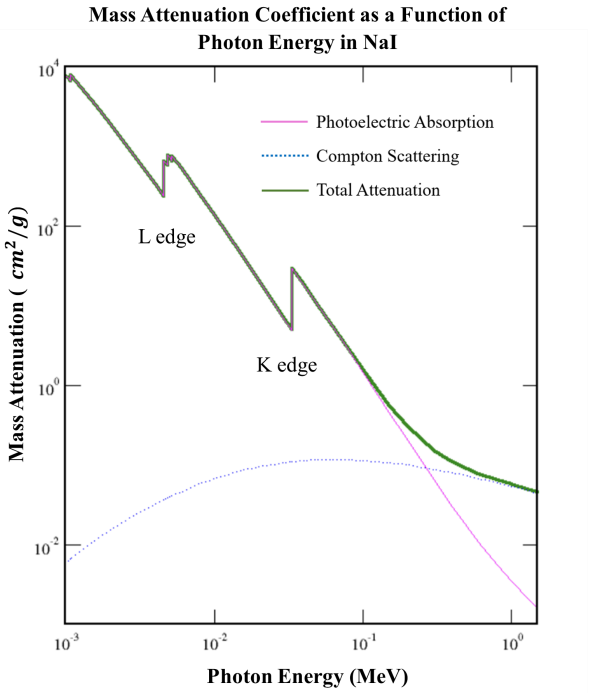

Figure 2.1: Log scale mass attenuation as a function of photon energy in NaI crystals. Increase in photoelectric absorption cross section at K and L edges where photon energy matches the K shell electron and L shell electron binding energies respectively. (From 'XCOM', available here: https://physics.nist.gov/PhysRefData/Xcom/html/xcom1.html.)

2.3 Photomultiplier (PM) Tube

Following the scintillator crystal is the PM tube, which converts the light output from the scintillator to an electrical signal. Photomultiplier tubes may have very high sensitivity to light with the capability of converting single photon light pulses to electrical signals [6]. The scintillator crystal may be connected via light pipes, placed directly on top, or coupled with a silicon-like material that does not infringe upon the propagation of light to inside the PM tube [7].

On entering the evacuated enclosure, photons from the scintillator reach the photocathode, where they are absorbed through the photoelectric effect. An electron which has absorbed such a photon will be promoted to higher energy levels, and, provided the incident photon has sufficient energy, it can possess kinetic energy greater than the work function, allowing for the escape of the electron from the photocathode entirely. Thallium doped sodium iodide scintillators have an emission peak of approximately 400 nm light, or around 3 eV, and hence electrons can overcome the work function of a photocathode, which may lie at 2 eV [8][2]. The free electrons are focused with electrodes towards the dynodes, where electron multiplication begins. Analogous to the photoelectric effect, an electron incident on a dynode may deposit its energy to eject more than one electron from the dynode material. Due to the low energy of the first incident electron, the first dynode is held at a high, positive potential, set by the power supply, to increase the kinetic energy of the electron. The accelerating voltage experienced by this electron can be hundreds of volts, for which theoretically could produce hundreds of electrons in turn. However, due to the random motion of freed electrons in the dynode material, not all will overcome the work function of the dynode material, and hence less electrons are ejected from the first dynode than theory predicts. This process repeats for subsequent dynodes, each held at a higher potential, where electrons ejected from previous dynodes are accelerated to the next for electron multiplication.

Electrons may also be ejected from the photocathode and dynodes through thermionic emission, and produce output signals in the absence of light called dark noise. Fortunately, this noise is dwarfed during the detection of true light pulses, due to the production of large orders of magnitudes of electrons, potentially 10^5 to 10^7 [9]. At the end of the series of dynodes is the anode, where the electrons are collected, resulting in a detectable sharp current pulse. The anode output is typically used for timing experiments, whereas the last dynode signal is sent for readout in gamma-ray spectroscopy [10].

Typically, the photocathode and dynodes are supplied with a voltage by a single supply across a potential divider network. The power supply is often connected at the rear of the PM tube itself, or at a detachable base that may also contain additional circuitry such as a pre-amplifier. The photocathode is typically held at ground with the anode held at the highest potential, equal to the power supply output to create a large accelerating voltage. The potential difference across each dynode drives a current to replenish electrons lost from emission in the electron multiplication process. As the number of electrons ejected from the dynodes increases further down the chain, a greater current must be supplied to the latter dynodes. If their current draw increases to respectively large values, then their voltages will deviate from their standard levels, leading to fluctuations in PM tube gain. To combat this, although not a perfect solution, one introduces stabilising capacitors in parallel to the resistors in the potential divider network. These aim to supply current lost to the dynodes and recharge from the potential divider network [2].

3 Experimental Set-up

For the investigation of behaviour variations of NaI(Tl) scintillation detectors of different sizes, five detectors were investigated; 0.55″ x 1.69″, 1″ x 1″, 2″ x 2″, 3″ x 3″ and 4.49″ x 4.49″ crystals (ϕ x l). The 0.55″ x 1.69″ and 4.49″ x 4.49″ models are without PM tube bases, and hence require a separate pre-amplifier unit.

Each scintillation detector was mounted and positioned in front of a frame in which radioactive samples would be held. Each radioactive source was contained in a rectangular plastic case with an extended arm to reduce unnecessary exposure to radiation. The source-detector distance was measured as the distance between the front crystal face to the face of the source casing nearest the detector that was held in the frame. This distance was adjusted based on the size of the scintillator. Figure 3.1 provides a schematic of the set-up, with the components illustrated in a block diagram in figure 3.2.

The HV supply value was set based on the rating of each PM tube and ranged between 700 - 1000 V for the investigation. The amplifier gain was adjusted to a point where the spectra of radioactive sources was distributed as much as possible across the 2048 channels of the ADC without losing data at higher γ-ray energies. During the investigation of a particular detector, the voltage supply and gain settings were kept constant such that calibration data were reliable, in converting between channel numbers of the ADC to energy values in keV. The spectra were viewed on a PC running Maestro software, that provided key information such as live times and real times of data collection and counts in particular regions of interest. These were saved in ASCII format for analysis in the Linux environment via 'root' and for conversion to CSV files for fine data handling.

A sixth detector, self-activated cerium bromide ($CrBr_3$), was used for the investigation of anode and dynode signals as it is equipped with an additional BNC connection for a direct view of the anode output signal. This detector also required a separate pre-amplification unit.

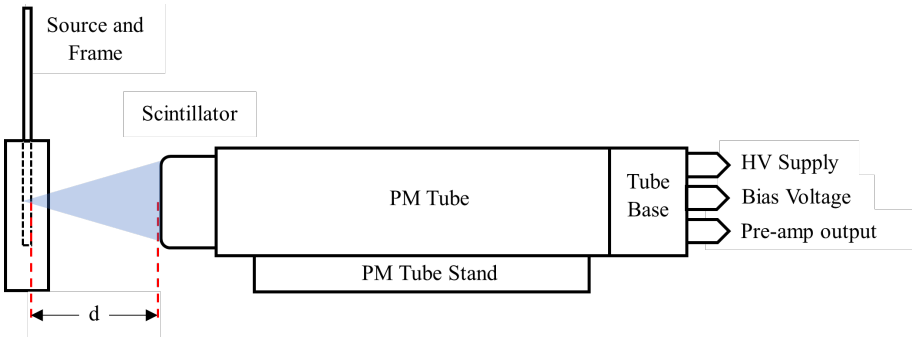

Figure 3.1: Schematic of experimental set-up for the investigation of different size NaI(Tl) scintillation detectors. The source-detector distance is denoted 'd'. Three connections are situated at the rear where a high voltage (HV) power supply is inputted, a bias voltage input, and a pre-amplifier output (only for PM tubes with bases) which is fed to a separate amplifier unit. For PM tubes without bases, the pre-amplifier is replaced with the last dynode signal that is sent to a separate pre-amplifier. The shaded conic projection represents the solid angle, Ω, subtended by the source to the scintillator face.

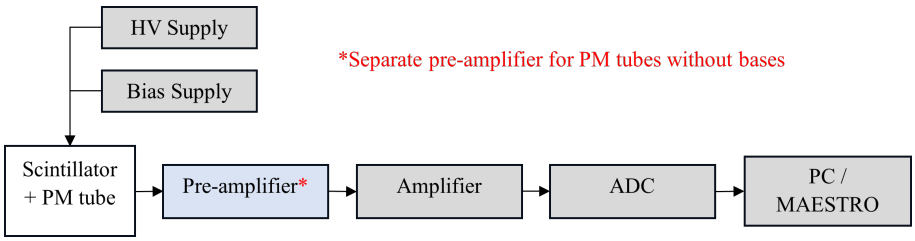

Figure 3.2: Block diagram of components for the investigation of different size NaI(Tl) scintillation detectors.

4 Preliminary Investigation

4.1 Calibration of 1 inch Detector

The first step was performing calibration, using the set-up illustrated in figure 3.1. For greater accuracy over the built-in calibration on Maestro, a linear fit was to be applied manually to the relation between channel numbers of full-energy peaks and the centroid energy of those peaks in keV, since ideal scintillation detectors are linear. The spectra were processed in root, where each full-energy peak was fitted with a Gaussian. The advantage of root was that it subtracted background readings by assuming a linear decay, which meant an accurate reading of counts was provided, in addition to the centroid channel number, and the FWHM. The data were recorded separately in an Excel workbook, which was subsequently transferred to a text file through Python where a least-squares fit program could fit the data.

A linear fit was not suitable initially, and the residuals illustrated large fluctuations, on the order of 100 channels, from the fit (figure 4.1a), which was both unexpected and concerning. On removing anomalous data points, the residuals improved significantly, yet the relationship was not linear. Closer inspection of photographic evidence of the set-up throughout the measurement period illustrated a change in the HV supply. It drifted from 700 V to 670 V, and returned to the desired value by the final measurements. With no means of isolating data which were taken under inconsistent conditions, the investigation was repeated. This emphasised the importance of ensuring the apparatus was operating at the desired settings to reduce possible sources of undesired effects.

Despite repeating the calibration process, the relationship between channel number and

energy was not linear. The residuals exhibited positive curvature at higher energies, suggesting that a quadratic fit was more appropriate. Figure 4.1b illustrates this non-linear behaviour. With greater confidence in the detector operation, the non-linearity could be associated with internal effects with greater certainty. Calibrating the 1 inch detector demonstrated that not all detectors would necessarily behave linearly. Jaffe et al. confirm non-linearity as an almost expected effect seen in scintillation detectors, particularly alkali activated monohalides such as NaI(Tl) [11]. A major drawback of this non-linearity is the need for a larger set of radioactive samples for calibration that cover a wide range of energies. This is particularly problematic for detectors of lower resolution where not every full-energy peak will be visible. With fewer data points for a quadratic calibration, one can be less certain if a fit has converged sufficiently well to the true behaviour.

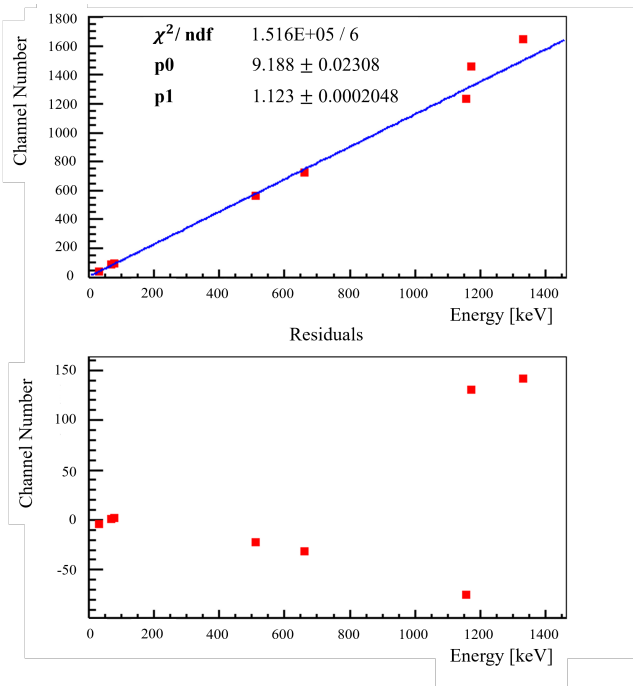

(a) Initial linear fit for calibration of the 1 inch scintillation detector with larger deviations visible at larger energies. Residuals further support this deviation beneath the plot, reaching 150 channels at higher energies.

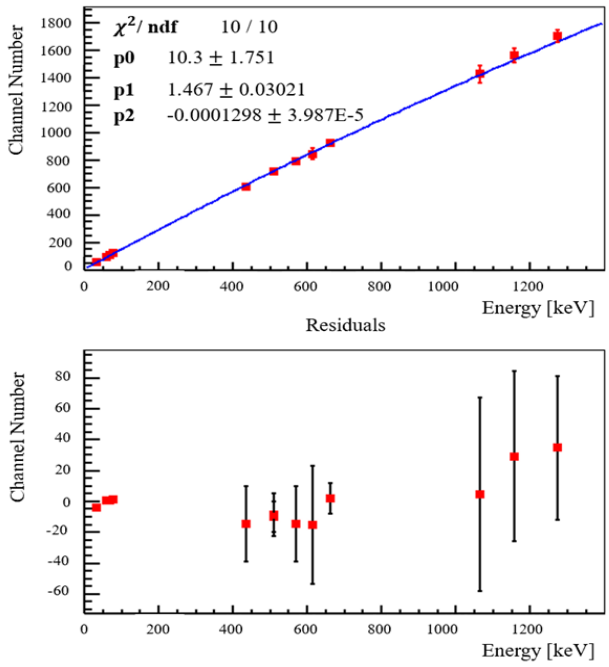

(b) Improved quadratic calibration fit for the 1 inch detector with improved error magnitudes. χ^2 reduced to one from error scaling and residuals fluctuate less than previously around the zero value.

Figure 4.1: Initial calibration plots of the 1 inch scintillation detector

The χ^2 value for the quadratic fit is one, by design, as the magnitude of the errors gathered from root were increased by a scaling factor of $\sqrt{\tilde{\chi}^2/N_{df}}$, where N_{df} is the number of degrees of freedom and $\tilde{\chi}^2$ is the chi-squared value of the unscaled data. This was necessary as the the original χ^2 value would be several orders of magnitude larger due to the nature of the fitting program; it assumes the data provided, i.e. a spectrum, represents a large number of repeat readings, and hence underestimates the error on the best fit parameters. Any subsequent deviation from the fit would therefore result in a large χ^2 value. By scaling, one can also perform more suitable error propagation if the fit is required for further analysis.

4.2 Resolution of 1 inch Detector

Having calibrated the 1 inch detector, the FWHM of each Gaussian fitted to a full-energy peak could be determined in keVs that would allow for detector resolution calculations. Energy

resolution relates to the broadness of photopeaks, and hence FWHM is best for quantifying resolution. A width of a particular peak illustrates that despite monoenergetic γ-rays for a particular decay entering the scintillation crystal, different energies have been recorded for the same event. Statistical noise can be a dominant effect, where broadening of peaks occurs due to characteristic fluctuations in electrons received at the end of electron multiplication [2]. If one assumes these fluctuations to follow a Poisson distribution, then, under large N electrons, the distribution will approximate to be Gaussian. Considering the ideal case where detectors are linear, the centroid photopeak energy, E_c, is proportional to N. The standard deviation σ is therefore proportional to $\sqrt{N}$. The energy resolution is defined as,

$$R \equiv \frac{FWHM}{E_c}, \tag{1}$$

and hence $R \propto 1/\sqrt{N}$, or $\log R \propto -\frac{1}{2}\log N$. A log-scale plot of the energy resolution of the 1 inch scintillation detector should yield a straight line of gradient -0.5. Figure 4.2 illustrates the resolution plot on log-scale of the 1 inch scintillation detector. The linear fit has a negative gradient of magnitude 0.4148, shallower than one would expect from theory considering only Poisson statistics. With -0.5 lying slightly outside two confidence intervals, one expects other factors at play for this gradient which are causing a loss in resolution since the magnitude of resolutions at higher energies are not decreasing at a faster rate. Iredale highlights that intrinsic crystal resolution, which is yet to be fully understood, is greatly effected by the non-proportional response of NaI(Tl) to electrons [12]. The variations in the number of electrons involved in the scintillation process from the total absorption of a γ-ray contributes much more significantly to resolution loss than other detector characteristics such as the PM tube photocathode efficiency.

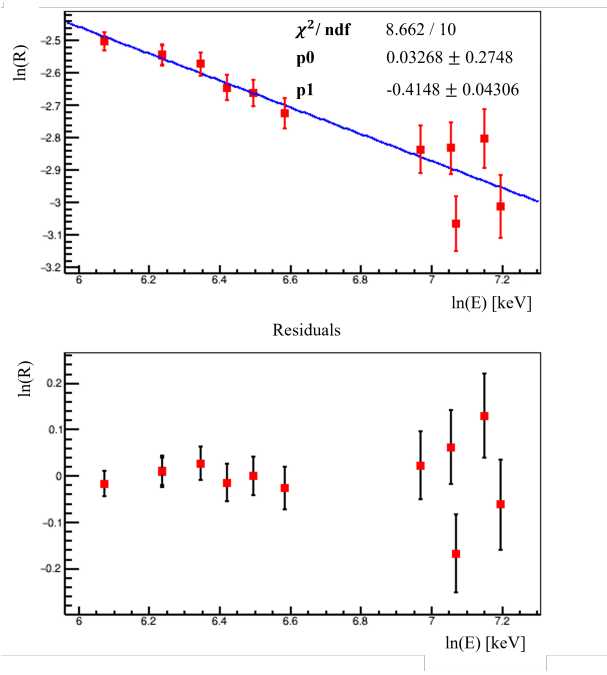

Figure 4.2: Log-scale resolution plot of the 1 inch scintillation detector as a function of energy. Larger deviations are seen above ~1000 keV possibly linked to non-proportionality of light yield. Detector ageing is also considered as an influencer in this non-proportionality.

A resolution of 6.99 ± 0.21% is seen for 662 keV γ-rays which appears to compare well with other literature values, such as the 11.18% seen by Singh et al. for a 1″ x 1″ NaI(Tl) scintillator [13]. However, the doping concentration of Tl in their scintillator was between 0.1% and 0.5%, which is lower than 1% which seems to provide optimal light yield and hence an improved

resolution [14]. The detector in this investigation may have a doping concentration that would provide a superior resolution.

4.3 Efficiency of 1 inch Detector

Having examined the resolution of the 1″ x 1″ detector and gaining insight to potential non-linearities, the relationship between intrinsic efficiency and γ-ray energy was explored. Intrinsic efficiency was chosen over absolute efficiency, since the former does not include the solid angle subtended by the detector and allows for a direct comparison between different sized detectors. The relationship between intrinsic and absolute efficiency is given below in equation 2,

$$\epsilon_{intr} = \frac{4\pi}{\Omega}\epsilon_{abs}, \tag{2}$$

where Ω is the solid angle. The absolute efficiency is given by equation 3,

$$\epsilon_{abs} = \frac{N}{\gamma A t}, \tag{3}$$

where N is the number of counts for a given full-energy peak, γ the intensity of the full-energy peak (available from official records), and t the live time of the spectrum collection. Live time was used instead of real time, as the former only includes the time where data collection was occurring, excluding any time when the PM tube was overloaded and processing signals.

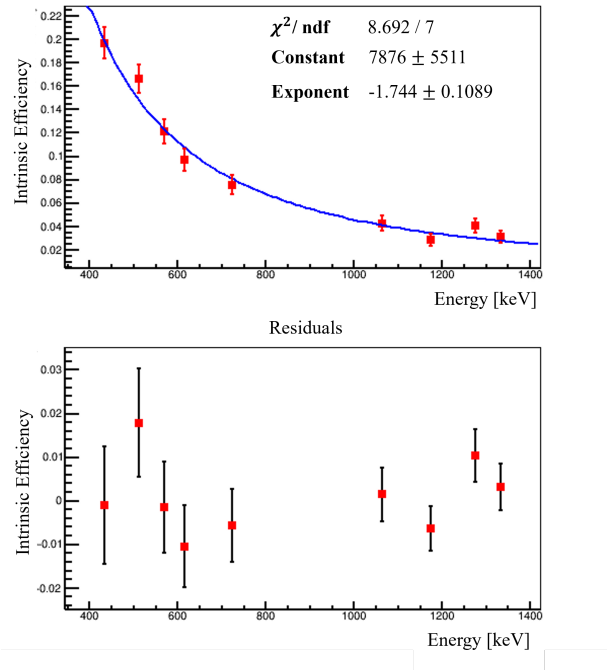

Figure 4.3: Efficiency of the 1″ x 1″ scintillator as a function of γ-ray energy.

Figure 4.3 illustrates the efficiency plot for the 1 inch detector. A power law was fitted, with good success as demonstrated by the low χ^2 value of 8.629, and little fluctuation in residuals around the zero value. On closer inspection at the lower energy range, slight curvature is seen at the top. Data for lower energy γ-rays had to be omitted, such as the 59.5 keV full-energy peak from Am-241, since the efficiency increases with energy before reaching a peak, typically around 100 keV before reducing by a power law, as seen in the figure. For the 1 inch detector, the intrinsic efficiency, $\epsilon_{intr} \propto E^{-1.744}$. The exponent relates to the interaction of γ-rays with the NaI crystal as discussed in section 2.2. If one were to see an exponent

near -3.5, photoelectric absorption would be the most dominant process in contributing to the number of counts detected (and an exponent near -1 for Compton scattering dominating). As the exponent is in between these values, both photoelectric absorption and Compton scattering are contributing to the counts detected.

5 Main Investigation

5.1 Comparison of Detector Resolutions

Well-functioning scintillation detectors will lose resolution primarily from the Poisson statistical broadening of full-energy peaks. As previously established, this would result in a gradient on a log scale plot of -0.5. Figure 5.1 illustrates the resolution as a function of γ-ray energy for the five NaI(Tl) detectors. One sees little variation between the resolution change in the 1″, 2″, and 3″ detectors, with the foremost and the latter behaving almost perfectly parallel to one another. The magnitude of the gradients of the resolution plots for these three are slightly below 0.5, suggesting there are other sources of resolution loss, since the resolution values will now be marginally higher than anticipated. As explored in section 4.2, detector ageing may be a factor in resolution loss as there seems to be a strong indication of non-proportional light yield in the 1″ detector; since the 2″ and 3″ detectors behave in a similar way, this could indicate potential non-proportional light yield within these. Larger fluctuations are seen at higher energies, particularly for the 1″ x 1″ detector, which potentially reflects the spread in total light output produced due to scattering at this higher range.

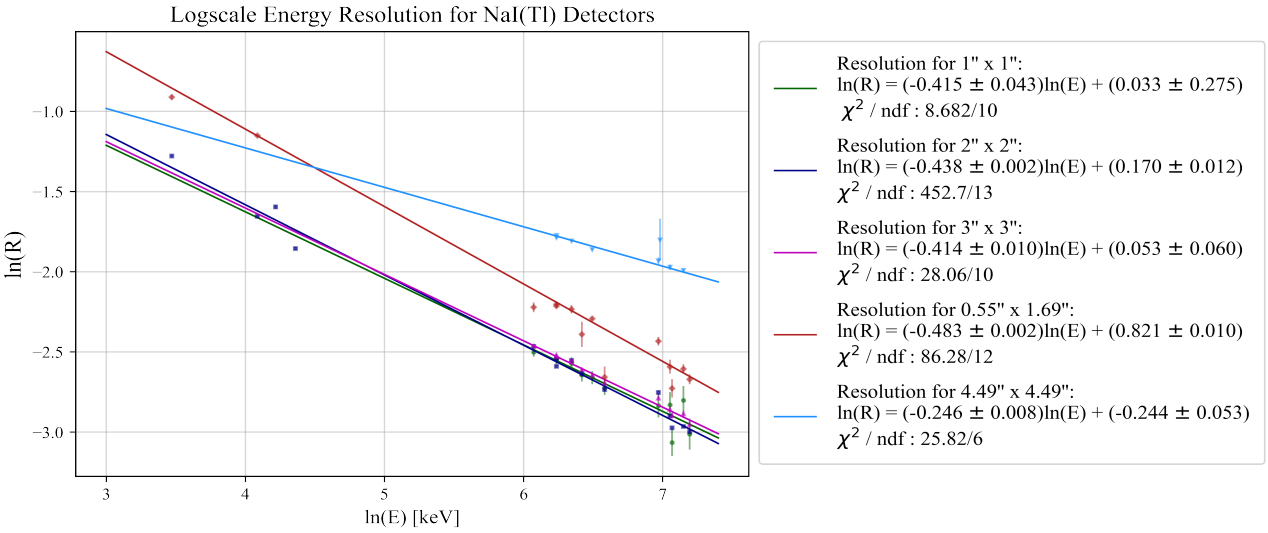

Figure 5.1: Resolution of five different sized NaI(Tl) detectors.

The 0.55″ x 1.69″ detector has a gradient nearest the theoretical value under the statistical broadening regime, of -0.483; this suggests that Poisson statistics has a large contribution in resolution loss. Overall, the resolution is significantly worse than the 1″, 2″ and 3″, as seen in table 1. This suggests little relationship between scintillator crystal size and resolution, as supported by Mengesha et al. and Moszyński et al. in their comparison between ϕ 1 cm x 1 cm and ϕ 7.5 cm x 7.5 cm crystals [15][16].

The largest detector, 4.49″ x 4.49″, has the smallest magnitude gradient in its resolution plot of 0.246. This strongly suggests external factors such as crystal age are significantly reducing the energy resolution over statistical broadening. This was to be expected as many full-energy peaks could not be resolved, hence the absence of data for Co-60 in table 1. An experimental

difficulty in determining the resolution of the largest detector was achieving sufficiently high gain to occupy as many channels as possible on the ADC; approximately half the number were accessible compared to the previous four investigated, making curve fitting more challenging.

Table 1: Quoted Energy Resolution percentage values for different NaI(Tl) Scintllators.

Radioisotopes	NaI(Tl) Dimensions (ϕ x l)				
	0.55″ x 1.69″	1″ x 1″	2″ x 2″	3″ x 3″	4.49″ x 4.49″
Cs-137 (662 keV)	10.09 ± 0.08	6.99 ± 0.29	6.89 ± 0.09	7.08 ± 0.07	15.55 ± 0.08
Co-60 (1332 keV)	6.92 ± 0.22	4.91 ± 0.48	4.99 ± 0.05	5.22 ± 0.10	...

5.2 Comparison of Detector Efficiencies

Intrinsic efficiency of NaI(Tl) crystals was shown to increase with detector size as expected (figure 5.2). The largest detector was an exception to this trend, which is less surprising when considering its resolution and the highly likely detrimental impacts that crystal imperfections and possibly ageing PM tube are having; this particularly supports the possibility of poor light yield within the crystal itself. Table 2 illustrates this increasing efficiency trend for Cs-137 and Co-60 full-energy peaks.

As discussed in section 4.3, photoelectric absorption and Compton scattering are the main components contributing to the efficiency. The efficiency and best-fit exponent of the 0.55″ is very near that of the 1″ detector, despite being roughly half the diameter. This suggests a dependence on depth of the crystal, as the 0.55″ detector is 1.69 times that of the 1″ detector. This may reduce the escape of small angle scattered photons and those in the forward direction hence increasing the efficiency. With increasing diameter, the exponent of the energy approaches unity, demonstrating the more significant role of Compton scattering over photoelectric absorption, increasing the number of counts detected at higher energies and hence improving the efficiency.

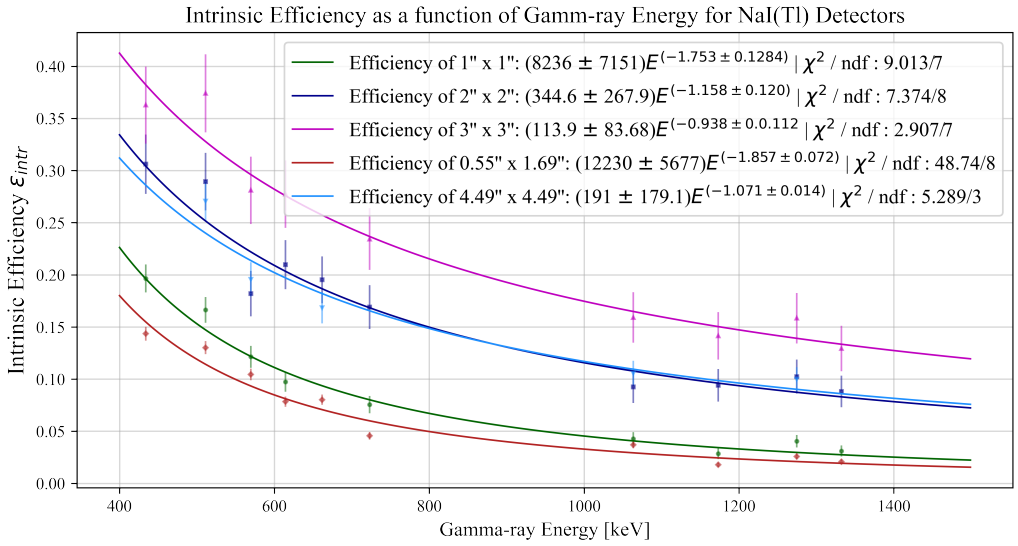

Figure 5.2: Efficiency of five different sized NaI(Tl) detectors.

Table 2: Quoted Efficiency Percentage values for different size NaI(Tl) Scintllators.

Radioisotopes	NaI(Tl) Dimensions (ϕ x l)				
	0.55″ x 1.69″	1″ x 1″	2″ x 2″	3″ x 3″	4.49″ x 4.49″
Cs-137 (662 keV)	8.02 ± 0.49	9.35 ± 0.94	19.52 ± 2.25	27.10 ± 3.14	16.86 ± 1.50
Co-60 (1332 keV)	2.07 ± 0.25	3.10 ± 0.53	8.82 ± 1.51	12.93 ± 2.18	...

5.3 Comparison of Photopeak-to-Compton Ratios of Detectors

The Compton continuum, as discussed in section 2.2, can be detrimental to low energy photopeaks which may lie on top. This can reduce the distinguishability of full-energy peaks, and their Gaussian shape, leading to inaccurate calibration points and resolution values; this impact was seen on the 59.5 keV peak from Am-241. The effect of the continuum reduces with increasing scintillator size. In the theoretical limit of an infinitely sized scintillator, all γ-rays will be captured without possibility of backscattering from the PM tube. This relationship was aimed to be found experimentally by comparing the photopeak-to-Compton ratio of the five scintillators for Cs-137. This radioisotope was chosen since the spectrum has one full-energy peak approximated well to a Gaussian and one Compton edge. The source used also had an x-ray shield to remove the need for extra peak fitting.

Compton backscatter had to be removed in order to obtain counts from the Compton continuum alone. The continuum was assumed to be linear beneath the backscatter and several linear fits were applied, giving an average. This process is illustrated for the 1″ x 1″ detector in figure 5.3a. The backscatter region was then isolated, with any datum exceeding the linear fit being capped to the value of the fit at that point. The remaining spectrum did not represent the random nature of counts collected and hence Gaussian noise was added to the data in the trimmed backscatter region. The noise was drawn from a normal distribution of mean zero and standard deviation of 15, which was adjusted depending on the scatter of an entire spectrum. The resulting spectrum for the 1″ detector is illustrated in figure 5.3b.

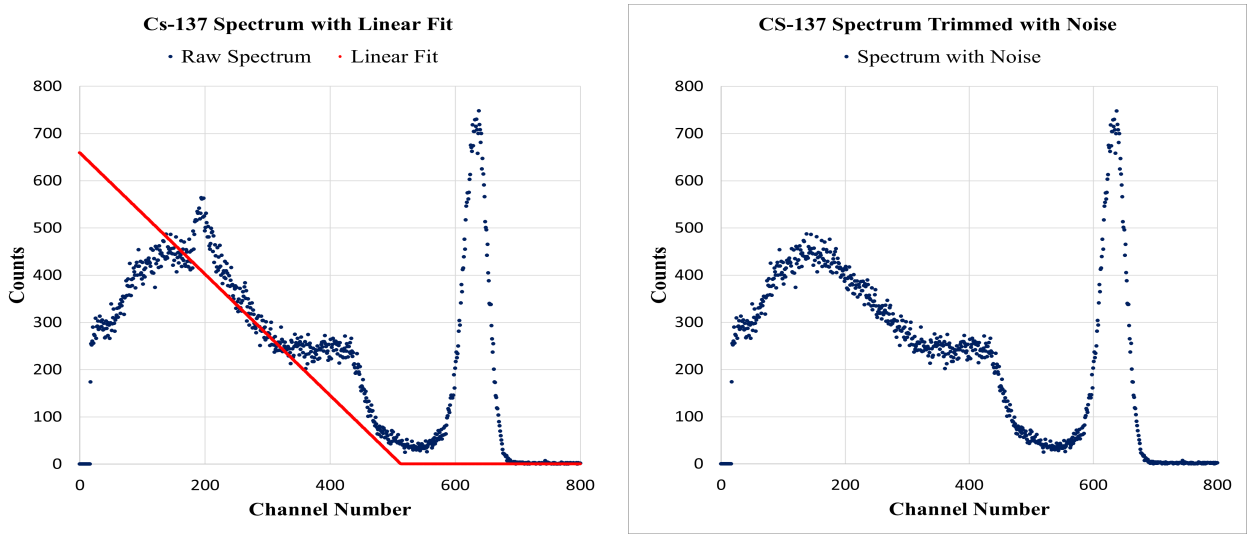

(a) Caesium-137 scatter spectrum with a mean linear fit estimating the shape of the Compton continuum without Compton backscatter.

(b) Caesium-137 scatter spectrum with Gaussian noise added to the linear region to simulate fluctuations from the detector.

Figure 5.3: Illustration of backscatter removal process for the 1″ x 1″ scintillation detector that was repeated for all detectors.

The results are tabulated below in table 3. As expected, the Compton continuum reduced

relative to the full-energy peak, therefore increasing the photopeak-to-Compton ratio with increasing scintillator size. Every detector gives rise to a Compton continuum greater than the 662 keV full-energy peak, with the 3″ x 3″ performing the best. The fact that the largest detector has a lower ratio than the 3″ is further evidence that there is some defective behaviour inside.

Table 3: Photopeak-to-Compton ratio of NaI(Tl) crystals of different sizes.

Photopeak-to-Compton Ratio of NaI(Tl) Scintillators		
Scintillator Dimensions, ϕ x l (inches)	Photopeak-to-Compton Ratio, N_{ph}/N_C	Error on Ratio
0.55 x 1.69	0.151	0.001
1 x 1	0.233	0.001
2 x 2	0.441	0.001
3 x 3	0.580	0.002
4.49 x 4.49	0.506	0.003

5.4 Anode and Dynode signals of $CeBr_3$ Scintillation Detector

The gain of the final dynode was to be determined by comparing voltage signals at the dynode and anode, that was held near ground (in contrast to the NaI(Tl) detectors whose anodes were at a high positive potential set by the power supply). Now the photocathode was at a high magnitude negative potential to maintain the acceleration of electrons to the series of dynodes. The use of negative high voltage is most convenient when the anode is directly coupled to an external circuit and allows for the photocurrent to be measured at the low voltage end of the circuit [17]. Figure 5.4 illustrates a sample of the anode and dynode signals from the detector.

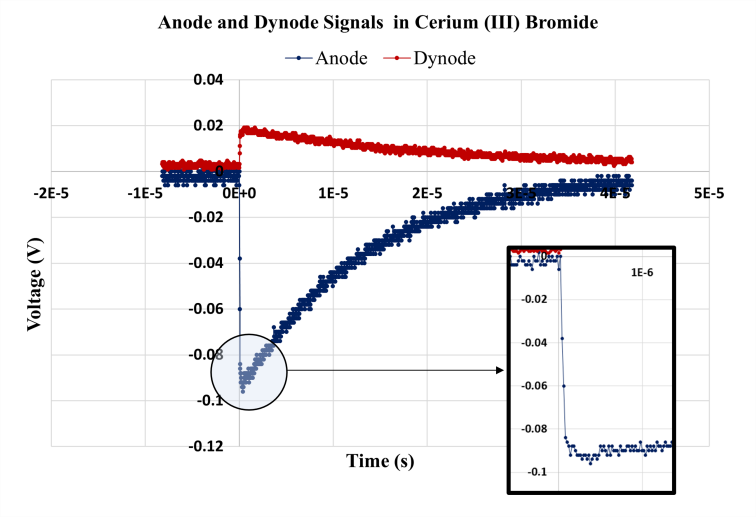

Figure 5.4: Anode and dynode signals from $CeBr_3$ scintillation detector.

The last dynode signal is of positive polarity whereas the anode is negative in polarity. This opposing behaviour is due to the opposite flow of electrons; the anode is being read out hence there is a potential drop, whereas electrons are flowing to the dynodes to replenish lost charge in electron multiplication. The anode has a parasitic capacitance, C, in parallel with a resistance, R, giving a time constant $\tau = RC$. The current flowing to the anode RC circuit is dependent on the total charge collected over one event, Q, and the decay time (as discussed in section 2.1) of the scintillator, λ [2].

$$i(t) = \lambda Q e^{-\lambda t}. \tag{4}$$

This current splits as it flows through the resistor and capacitor, resulting in an output voltage of,

$$V(t) = \frac{1}{\lambda - 1/\tau}\frac{\lambda Q}{C}(e^{-t/\tau} - e^{-\lambda t}). \tag{5}$$

One sees from this that if the decay time of the scintillator is much larger than the time constant, the rising behaviour of the pulse is dominated by λ, and a longer rise time would be observed. From the enlarged view in figure 5.4, one sees a very short rise time, suggesting that the scintillation decay time is much smaller than the time constant of the parasitic capacitance. This is favourable in fast timing experiments. The time constant of the anode RC circuit is smaller than the final dynode time constant, as seen from the less sharp decay, which is likely caused by the stabilising capacitors. Defining the decay time of the anode and dynode pulses to be the time taken for the voltage pulse to reach 1/e the maximum value, the mean decay times for the anode and dynode signals were found to be (13.47 ± 0.08) μs and (27.71 ± 0.57) μs respectively; the anode pulse decay time is half that of the last dynode. As established in section 2.1 the scintillator decay time, λ, will be on the order of ns, further supporting that the time constant of the anode RC circuit is much greater than λ.

If n electrons arrive at the last dynode, and $n\alpha$ electrons leave the last dynode, the gain at the last stage is given by $g = \alpha - 1$. The factor α was determined by taking the ratio of the maximum pulse heights of the anode and dynode and calculated for photocathode voltages of -1000 V, -800 V, -700 V with the results tabulated below in table 4.

Table 4: Last dynode gain for different photocathode voltages.

Factor	Photocathode Voltage (V)		
	-1000	-800	-700
g	4.82 ± 0.03	4.37 ± 0.03	4.05 ± 0.05

With the PM tube rated for -1000 V and not being operable at -600 V, finding a relationship between g and the photocathode voltage was not possible beyond the expected decrease in gain with decreasing photocathode voltage. The data were recorded by monitoring pulses from Am-241. The source was changed to Cs-137 that had a lower activity to compare the effects of activity on gain. At -1000 V, the gain at the last dynode was 4.84 ± 0.05, almost exactly as before with Am-241. This supports the claim that the dynode gain is independent of the activity of the source under investigation, as one would expect, otherwise fluctuations in gain would be seen leading to meaningless calibration plots. Furthermore it demonstrates that the PM tube was not overwhelmed with a high activity source, meaning that one would expect respectably low dead times in recording majority of spectra.

6 Conclusions

Five NaI(Tl) scintillation detectors of different sizes have been characterised, with a focus on resolution and efficiency as a function of γ-ray energy, and on photopeak-to-Compton ratio for 662 keV full-energy peaks. Non-linearities seen from the calibration of the 0.55″ x 1.69″, 1″ x 1″ and 3″ x 3″ have been attributed mainly to ageing where light yield non-proportionality has had a more significant impact on resolution loss, as supported by shallower gradients, illustrated in figure 5.1. No clear relationship between detector size and resolution was seen from this sample of detectors which is in agreement with Mengesha et al. and Moszyński et al. [15][16]. There is some indication of increase in resolution with detector size albeit negligible, particularly for 662 keV full-energy peaks. Although resolution increased for the largest detector as seen in

table 1, this is likely due to non-proportional light yield since its intrinsic efficiency was lower than that of the 3″ x 3″.

A much clearer relationship was seen with increasing detector size and increasing intrinsic efficiency. This was related to photon interactions in the NaI(Tl) crystals, where dominant Compton scattering events at higher energies would escape less for larger detectors. The exponents of the energy in the efficiency fits supported this, with exponents nearer unity in magnitude for the larger detectors (reflecting the inverse energy dependence), and greater magnitude exponents for smaller detectors reflecting the greater contribution of photoelectric absorption. Since Compton scattering events were much more likely to escape in these, the efficiency decayed at a faster rate for higher energy γ-rays.

Photopeak-to-Compton ratio was also seen to increase with increasing detector size, for similar reasons to efficiency increase with larger detectors. With a lower probability of γ-rays escaping larger crystals, there is a greater likelihood of a photon depositing all its energy to a photopeak, leading to a smaller continuum with respect to full-energy peaks, which was confirmed in table 3. The largest detector was an outlier in this trend which is less surprising when considering its resolution and intrinsic efficiency variation with energy. This further supports that non-proportionality of light yield greatly effects this detector in particular.

The comparison between the anode and dynode signals from the $CeBr_3$ detector showed a faster decay time by approximately a factor of two for anode signals for a given event compared to the dynode (13.47 ± 0.08 μs compared to 27.71 ± 0.57 μs), hence illustrating both the suitability of this detector in fast timing experiments and that the decay time of the scintillator is much less than the time constant of the RC circuit formed from the parasitic capacitance of the anode itself. The longer decay times of the dynode pulses was attributed to the stabilising capacitors that form RC circuits with the potential divider network. The maximum gain between the last dynode and the anode was 4.82 ± 0.03, and as expected, under the maximum applied negative voltage to the photocathode.

References

[1] Nassalski A, Kapusta M, Batsch T, Wolski D, Mockel D, Enghardt W, et al. Comparative study of scintillators for PET/CT detectors. In: IEEE Nuclear Science Symposium Conference Record, 2005. vol. 5; 2005. p. 2823-9.

[2] Knoll GF. Radiation detection and measurement. John Wiley & Sons; 2010.

[3] Galbiati C, Pocar A, Franco D, Ianni A, Cadonati L, Schönert S. Cosmogenic ^{11}C production and sensitivity of organic scintillator detectors to *pep* and CNO neutrinos. Phys Rev C. 2005 May;71:055805. Available from: https://link.aps.org/doi/10.1103/PhysRevC.71.055805.

[4] Schweitzer JS, Ziehl W. Temperature Dependence of NaI(Tl) Decay Constant. IEEE Transactions on Nuclear Science. 1983;30(1):380-2.

[5] Miyata T. Exciton Structure of NaI and NaBr. Journal of the Physical Society of Japan. 1969;27(1):266-6.

[6] Das MB, Bose S, Bhattacharya R. Single photon response of photomultiplier tubes. Nuclear Instruments and Methods in Physics Research Section A: Accelerators, Spectrometers, Detectors and Associated Equipment. 1985;242(1):156-9. Available from: https://www.sciencedirect.com/science/article/pii/0168900285909027.

[7] Mettler FA, Guiberteau MJ. 2 - Instrumentation and Quality Control. In: Mettler FA, Guiberteau MJ, editors. Essentials of Nuclear Medicine Imaging (Sixth Edition). sixth edition ed. Philadelphia: W.B. Saunders; 2012. p. 32. Available from: https://www.sciencedirect.com/science/article/pii/B9781455701049000020.

[8] Choi JJ, Park BJ, Ha C, Kim KW, Kim SK, Kim YD, et al. Improving the light collection using a new NaI(Tl) crystal encapsulation. Nuclear Instruments and Methods in Physics Research Section A: Accelerators, Spectrometers, Detectors and Associated Equipment. 2020;981:1. Available from: https://www.sciencedirect.com/science/article/pii/S0168900220309530.

[9] Eberhardt EH. Noise in Photomultiplier Tubes. IEEE Transactions on Nuclear Science. 1967;14(2):1.

[10] Zhang N, Thompson CJ, Togane D, Cayouette F, Nguyen KQ. Anode position and last dynode timing circuits for dual-layer BGO scintillator with PS-PMT based modular PET detectors. IEEE Transactions on Nuclear Science. 2002;49(5):2203-7.

[11] Jaffe JE, Jordan DV, Peurrung AJ. Energy nonlinearity in radiation detection materials: Causes and consequences. Nuclear Instruments and Methods in Physics Research Section A: Accelerators, Spectrometers, Detectors and Associated Equipment. 2007;570(1):72-83. Available from: https://www.sciencedirect.com/science/article/pii/S0168900206017578.

[12] Iredale P. The effect of the non-proportional response of NaI(Tl) crystals to electrons upon the resolution for γ-rays. Nuclear Instruments and Methods. 1961;11:340-6. Available from: https://www.sciencedirect.com/science/article/pii/0029554X61900362.

[13] Singh I, Singh B, Sandhu B, Sabharwal AD. Comparative study for intermediate crystal size of NaI(Tl) scintillation detector. The Review of scientific instruments. 2020 July;91(7):073105. Available from: https://doi.org/10.1063/5.0005243.

[14] Hofstadter R. The Detection of Gamma-Rays with Thallium-Activated Sodium Iodide Crystals. Phys Rev. 1949 Mar;75:796-810. Available from: https://link.aps.org/doi/10.1103/PhysRev.75.796.

[15] Mengesha W, Valentine JD. Benchmarking NaI(Tl) electron energy resolution measurements. IEEE Transactions on Nuclear Science. 2002;49(5):2420-6.

[16] Moszyński M, Zalipska J, Balcerzyk M, Kapusta M, Mengesha W, Valentine JD. Intrinsic energy resolution of NaI(Tl). Nuclear Instruments and Methods in Physics Research Section A: Accelerators, Spectrometers, Detectors and Associated Equipment. 2002;484(1):259-69. Available from: https://www.sciencedirect.com/science/article/pii/S0168900201019647.

[17] Adrián-Martínez S, Ageron M, Aiello S, Albert A, Ameli F, Anassontzis E, et al. A method to stabilise the performance of negatively fed KM3NeT photomultipliers. Journal of Instrumentation. 2016;11(12):P1.